

Dry and Moist Convection Forced by an Urban Heat Island

JONG-JIN BAIK AND YEON-HEE KIM

Department of Environmental Science and Engineering, Kwangju Institute of Science and Technology, Kwangju, Korea

HYE-YEONG CHUN

Department of Atmospheric Sciences and Global Environment Laboratory, Yonsei University, Seoul, Korea

(Manuscript received 22 May 2000, in final form 2 December 2000)

ABSTRACT

This study numerically investigates dry and moist convection forced by an urban heat island using a two-dimensional, nonhydrostatic, compressible model with explicit cloud microphysical processes (Advanced Regional Prediction System). The urban heat island is represented by specified heating. Extensive numerical experiments with various heating amplitudes, representing the intensity of the urban heat island, uniform basic-state wind speeds, and basic-state relative humidities, are performed to examine their roles in characterizing urban-induced convection. Two flow regimes can be identified in dry simulations. One regime is characterized only by stationary gravity waves near the heating region and is revealed when the urban heat island intensity is very weak. The other regime is characterized both by stationary gravity waves near the heating region and by a downwind updraft cell that moves in the downstream direction. The intensity of the downwind updraft cell increases as the heat island intensity increases or the basic-state wind speed decreases. Results of moist simulations demonstrate that the downwind updraft cell induced by the urban heat island can initiate moist convection and result in surface precipitation in the downstream region when the basic-state thermodynamic conditions are favorable. As the urban heat island intensity increases, the time required for the first cloud water (or rainwater) formation decreases and its horizontal location is closer to the heating center. It is shown that for the same basic-state wind speed and heat island intensity a stronger dynamic forcing—that is, a stronger downwind updraft—is needed to trigger moist convection in less favorable basic-state thermodynamic conditions.

1. Introduction

Many observational studies have indicated that cities can change or modify local and nearby weather and climate [see Changnon (1981) and Cotton and Pielke (1995)]. In particular, studies on urban-induced or urban-modified precipitation phenomena have been of interest because of their practical importance in urban water management as well as their scientific curiosity about convection and precipitation.

Changnon (1968) reported the precipitation anomaly at La Porte, which is located downwind of Chicago. His seminal study, which implied that human activity can inadvertently alter precipitation away from a city, has received much attention. Changnon et al. (1991) analyzed precipitation data collected at 116 rain gauges in the St. Louis area during a 4-yr period. They showed that precipitation was enhanced downwind of St. Louis by 17% and 4% during the autumn and spring seasons,

respectively. Bornstein and LeRoy (1990) analyzed radar echoes in the New York City area and documented the splitting of convective and frontal thunderstorms by urban barrier effects. Jauregui and Romales (1996) analyzed rainfall data in Mexico City to examine urban effects on convective precipitation. They found evidence of urban-induced increases in convective precipitation and pointed out that the frequency of intense rain showers has increased in recent decades. Events of urban-induced convective thunderstorms were recently documented by Bornstein and Lin (2000) using surface meteorological data in the Atlanta area. Their analysis of six precipitation events over the city for nine summer days revealed that the urban heat island induced a convergence zone that initiated three of the convective thunderstorms at different times of the day. A critical review of urban effects on precipitation amount is given by Lowry (1998).

These and other observational studies confirm that cities can initiate convection, split convective storms, change the behavior of convective precipitation, and enhance downstream precipitation. Some of the suggested causes for urban-induced precipitation changes include heat release into the urban atmosphere, in-

Corresponding author address: Prof. Jong-Jin Baik, Department of Environmental Science and Engineering, Kwangju Institute of Science and Technology, 1 Oryong-dong, Puk-gu, Kwangju 500-712, Korea.
E-mail: jjbaik@aromi.kjist.ac.kr

creased urban surface roughness, and anthropogenic condensation nuclei in the urban atmosphere (e.g., Changnon 1969). However, the basic understanding of the dynamics of urban-induced precipitation remains poor in spite of well-documented observations.

This study is concerned with dry and moist convection forced by the urban heat island and hence downwind precipitation enhancement in a dynamical viewpoint. Theoretical understanding of the precipitation enhancement observed downwind of the urban heat island is possible by examining the response of a stratified atmosphere to the specified thermal forcing that represents the heat island. The results of linear theoretical calculations in a stably stratified, uniform (Lin and Smith 1986) or shear (Baik 1992) flow suggest that there is downward motion near the heating center and there is upward motion downwind of the specified heating. This upward motion is partly attributed to the observed precipitation enhancement downwind of urban heat island (Lin and Smith 1986; Baik 1992). The weakly nonlinear theory proposed by Baik and Chun (1997) predicts that weak nonlinearity can induce upward or downward motion downwind of the specified heating, depending on the nondimensional heating depth. When the nondimensional heating depth is large, both a linear effect and a weakly nonlinear effect create upward motion downwind. This explains to a greater extent precipitation enhancement downwind than does the linear effect alone. Using a nonlinear dry numerical model that employs a hydrostatic, Boussinesq airflow system, Baik (1992) showed that when the heating amplitude is large, a strong updraft cell appears downwind of the specified heating. This updraft cell was suggested to be dynamically responsible for downwind precipitation enhancement.

This study extends our previous one (Baik 1992) by considering a nonhydrostatic, compressible airflow system, which is more appropriate for convection research, and by taking into account precipitation processes to investigate urban heat island-induced convection and precipitation in various environmental conditions. For the purpose of isolating the role of the urban heat island in urban-induced convection and precipitation, other potential factors (e.g., surface roughness effect) are not taken into account in this study. In section 2, a numerical cloud model used in this study is described and an experimental design for dry and moist simulations is given. In section 3, results from dry and moist simulations are given and discussed with regard to some dynamical aspects of urban heat island-induced convection and precipitation. A summary and conclusions follow in section 4.

2. Numerical model and experimental design

The numerical model used in this study is the Advanced Regional Prediction System (ARPS) developed at the Center for Analysis and Prediction of Storms

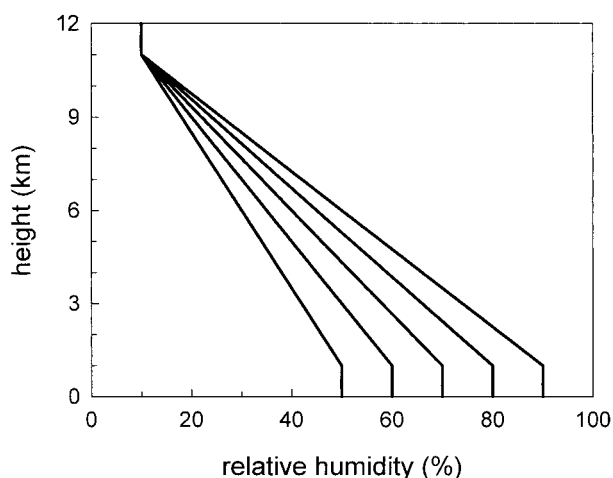


FIG. 1. The vertical profiles of the basic-state relative humidity used in moist simulations. The relative humidity is constant from the surface to $z = 1$ km, decreases linearly with height up to $z = 11$ km, and remains constant above, with $RH = 10\%$. The five profiles are for $RH_L = 50\%$, 60% , 70% , 80% , and 90% , where RH_L is the relative humidity in the layer between the surface and $z = 1$ km.

(CAPS), University of Oklahoma, by Xue et al. (1995). ARPS is a three-dimensional, nonhydrostatic, fully compressible, finite-difference model with complete physical parameterizations. In the current two-dimensional study, a flat surface is assumed and surface processes are neglected in order to examine dry and moist convection thermally forced by the presence of an urban heat island. Turbulent processes for momentum, heat, and water substances are parameterized using a 1.5-order turbulence closure scheme. Radiation processes are not considered. The rotational effect of the earth is neglected. In dry simulations, water substances are not included. In moist simulations, the mixing ratios of water vapor, cloud water, and rainwater are explicitly predicted with the bulk parameterization of cloud microphysical processes. Ice-phase cloud processes are not taken into account in this study. For further details of the numerical model, see Xue et al. (1995).

The basic-state wind speed U in the numerical simulations is considered to be uniform in the vertical and is set to 2, 3, 4, and 5 m s^{-1} . These low basic-state wind speeds are chosen because the urban heat island is well developed under the condition of weak winds (Oke 1987). The basic-state temperature profile follows that of the standard atmosphere, which is stable through the atmosphere. The vertical profiles of the basic-state relative humidity used in moist simulations are shown in Fig. 1. The relative humidity is constant from the surface to $z = 1$ km, decreases linearly with height up to $z = 11$ km, and is constant above, with $RH = 10\%$. The relative humidity in the layer between the surface and $z = 1$ km (RH_L) is set to 50%, 60%, 70%, 80%, and 90%. The physical domain sizes are 150 km in the horizontal and 12 km in the vertical. The horizontal and vertical grid intervals are 1 km and 150 m, respectively.

TABLE 1. A summary of the experimental design of numerical simulations conducted in this study.

	Basic-state wind speed (U , m s^{-1})	Heating amplitude (q_0 , $\text{J kg}^{-1} \text{s}^{-1}$)	Basic-state RH from surface to $z = 1 \text{ km}$ (RH_L , %)	No. of simulations
Dry simulations	2, 3, 4, 5	0.2, 0.4, 0.6, 0.8, 1, 1.2, 1.4, 1.6, 1.8, 2	No moisture	40
Moist simulations	3, 5	0.2, 0.4, 0.6, 0.8, 1, 1.2, 1.4, 1.6, 1.8, 2	50, 60, 70, 80, 90	100

A horizontal spacing of 1 km was shown to be adequate for simulating convective system using ARPS (e.g., Chun et al. 1999). To minimize the reflection of gravity waves at boundaries, a radiation boundary condition is employed at lateral boundaries and a sponge layer is put from $z = 12$ to 15 km , with height-dependent damping coefficients. With a large time step of 4 s and a small time step of 1 s (terms associated with acoustic waves), the model is integrated for 6 h.

To represent the urban heat island in the numerical model, the following thermal forcing is added in the thermodynamic energy equation:

$$\rho Q = \frac{\rho q_0}{c_p} \frac{a^2}{(x - c)^2 + a^2} e^{-z/h}, \quad (1)$$

where ρ is the air density, q_0 is the heating amplitude, c_p is the specific heat of air at constant pressure, a is the half-width of bell-shaped function, c is the horizontal location of the heating center from the left boundary, and h is the e -folding height. The specified heating (1), which is maintained during the time integration, decreases horizontally in a bell shape from the heating center and decreases exponentially with height. This heating structure roughly imitates the observed spatial temperature deviation pattern over cities. The heating center is located 50 km away from the left boundary ($x = 50 \text{ km}$), that is, $c = 50 \text{ km}$. The parameters a and h are specified as 10 km and 700 m, respectively. The parameter q_0 is considered to represent the intensity of the heat island and varies from 0.2 to $2 \text{ J kg}^{-1} \text{s}^{-1}$ in increments of $0.2 \text{ J kg}^{-1} \text{s}^{-1}$. The peak heating would be given by q_0/c_p , which corresponds to a heating rate of 0.7 to 7.1 K h^{-1} for a heating amplitude of 0.2 to $2 \text{ J kg}^{-1} \text{s}^{-1}$. A typical maximum difference in heating/cooling rate between urban and rural areas under ideal weather conditions is on the order of a few degrees per hour (Oke 1982). In this study, a wide range of heating amplitudes are chosen to examine extensively the effects of the urban heat island intensity. In comparison with observations, the lower and middle values in the chosen heating-amplitude range are reasonable, but the upper values may be large. One might consider that large heating amplitudes correspond to a future situation in which human activity further enhances urban heat island intensity. Table 1 summarizes the experimental design of numerical simulations conducted in this study.

3. Results and discussion

a. Dry simulations

To characterize urban heat island-induced dry convection in conditions of various heat island intensities and basic-state wind speeds, 40 dry simulations are performed with $q_0 = 0.2, 0.4, 0.6, \dots, 1.8$, and $2 \text{ J kg}^{-1} \text{s}^{-1}$ and $U = 2, 3, 4$, and 5 m s^{-1} (10 heating amplitudes $\times 4$ basic-state winds).

Figure 2 shows the perturbation vertical velocity fields at $t = 4 \text{ h}$ for heating amplitudes of $q_0 = 0.2, 0.4, 0.6, 0.8$, and $1 \text{ J kg}^{-1} \text{s}^{-1}$ with a basic-state wind speed U of 5 m s^{-1} . When the heating amplitude is small (Figs. 2a,b), the vertical velocity field is very similar to the linear internal gravity wave field induced by thermal forcing. Note that the basic-state atmosphere is stably stratified. Near the heating region, alternating upward and downward motions with an upstream phase tilt, implying the upward propagation of wave energy, are present. In the lower layer, downward motion exists in the region close to the heating center ($x = 50 \text{ km}$) and upwind. Also, a broad region of weak upward motion exists downwind of the heating center. The curious negative phase relationship between the heating and the induced vertical motion near the heating center is related to the steadiness (Smith and Lin 1982; Lin and Smith 1986; Baik 1992; Baik et al. 1999). The vertical wavelength of stationary gravity waves near the heating region in Fig. 2a is 3.3 km, which is close to that of linear, hydrostatic internal gravity waves ($2\pi U/N$, where N is the buoyancy frequency). As the heating amplitude increases further, the flow field gradually deviates from the linear response field (Figs. 2c–e). For the larger heating amplitude, there are two distinct modes: a stationary gravity wave field near the heating region and an (strong) updraft cell downwind of the heating center. The intensity of the downwind updraft cell increases with increasing heating amplitude. It is interesting to see downward and upward motions with an upstream phase tilt above the downwind updraft cell. These likely are maintained by the mechanical (momentum) forcing of the downwind updraft cell and move with the updraft cell. Their horizontal size is much smaller than that of the stationary gravity waves near the heating region because of the much smaller horizontal forcing scale of the downwind updraft cell.

The time evolution of the perturbation vertical velocity field in the $q_0 = 1.2 \text{ J kg}^{-1} \text{s}^{-1}$ and $U = 5 \text{ m s}^{-1}$

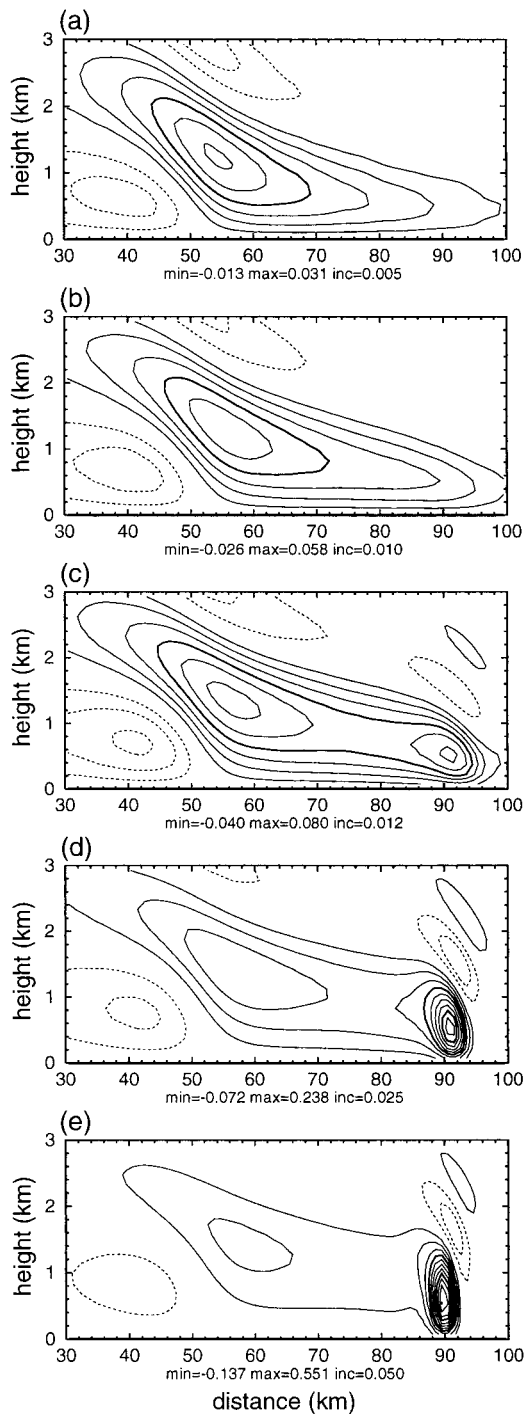
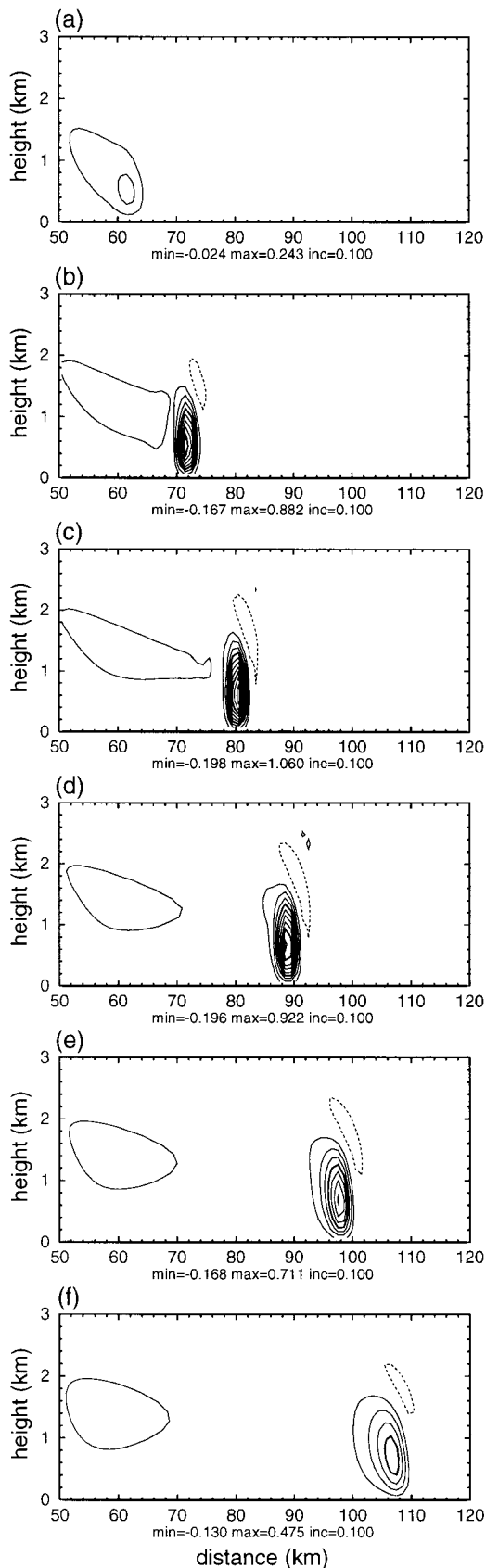


FIG. 2. Perturbation vertical velocity fields at $t = 4$ h for the heating amplitude $q_0 =$ (a) 0.2, (b) 0.4, (c) 0.6, (d) 0.8, and (e) $1 \text{ J kg}^{-1} \text{ s}^{-1}$ in dry simulations with a basic-state wind speed U of 5 m s^{-1} . In these and subsequent perturbation vertical velocity fields, the solid and dashed lines represent upward and downward motions, respectively, and zero-contour lines are not drawn. The min and max values and the contour interval (inc) are shown at the bottom of each frame (m s^{-1}). Note that the center of the urban heat island in all numerical simulations is located at $x = 50 \text{ km}$.

case is plotted in Fig. 3. At $t = 1$ h, the center of the downwind updraft cell is located at $x = 62 \text{ km}$ and the updraft cell with relatively weak intensity is not yet separated from the stationary gravity wave field near the heating region. The updraft cell continues to move downwind and strengthens its intensity. At $t = 2$ h, it is separated from the stationary gravity wave field and has a well-organized structure. The updraft cell further intensifies as it moves downwind ($t = 3$ h) and then gradually weakens as it moves downstream, owing to the dissipation effect ($t = 4, 5$, and 6 h). The maximum vertical velocities of the downwind updraft cell at 1, 2, 3, 4, 5, and 6 h are 0.24, 0.88, 1.06, 0.92, 0.71, and 0.48 m s^{-1} , respectively. The horizontal and vertical sizes of the separated downwind updraft cell are 4–10 and 1.5–2 km, respectively. The average moving speed of the downwind updraft cell is 2.5 m s^{-1} , that is, one-half of the basic-state wind speed. Note that stationary gravity waves exist near the heating region even if the updraft cell is away from the heating center (this can be confirmed with a smaller contour interval near the heating center).

Figure 4 is the same as Fig. 2 except that the basic-state wind speed is reduced from 5 to 3 m s^{-1} . In the $q_0 = 0.2 \text{ J kg}^{-1} \text{ s}^{-1}$ case (Fig. 4a), only a stationary gravity wave field is produced near the heating region. When the heating amplitude is $0.4 \text{ J kg}^{-1} \text{ s}^{-1}$, in addition to the stationary gravity wave field, an updraft cell can be identified near $x = 70 \text{ km}$. However, the updraft cell is weak and combined with the stationary gravity wave field. As the heating amplitude increases further (Figs. 4c–e), both stationary gravity waves near the heating region and a well-organized updraft cell downwind of the heating center are present. These flow characteristics with heating amplitude are similar to those in Fig. 2. In comparison with the cases having $U = 5 \text{ m s}^{-1}$ (Fig. 2), the vertical wavelength of the stationary gravity waves decreases and the updraft cell moves more slowly in the downstream direction because of the reduced basic-state wind speed.

Because of the specified steady heating, there is a horizontal temperature advection, and the horizontal temperature gradient differs for different basic-state wind speed and heating amplitude. An examination of the potential temperature fields corresponding to Figs. 2, 3, and 4 indicated that the downwind updraft cell forms in the region of strong horizontal temperature gradient. The strength of this temperature gradient is related to the steady heating amplitude. It is also related to the time experienced by flow at the heat source region, which in turn depends on the basic-state wind speed and the horizontal length scale of the heating. An examination of the potential temperature fields also indicated that the steady heating creates a more or less homogeneous horizontal temperature perturbation downstream of the heat source. This can prevent strong new updraft cells from being produced, despite the continuous heating upstream.



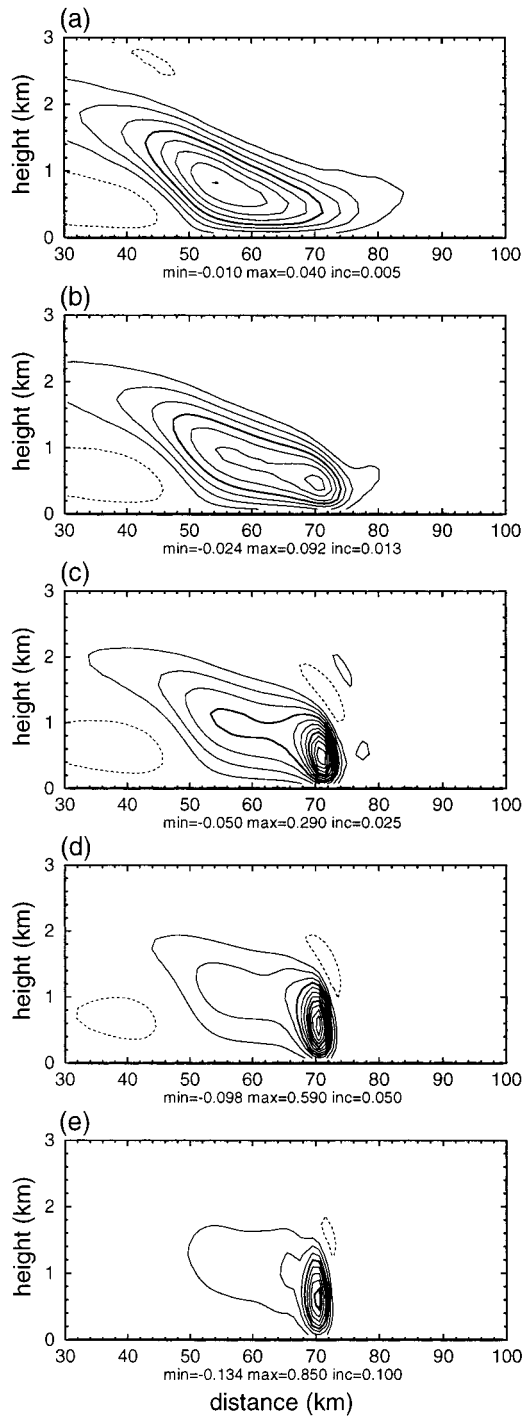
To examine the effects of the basic-state wind speed on the intensity of heating-induced perturbation, the domain-maximum perturbation vertical velocity during numerical simulation is plotted as a function of heating amplitude for $U = 2, 3, 4$, and 5 m s^{-1} (Fig. 5). For a given wind speed, the maximum vertical velocity increases as the heating amplitude increases. For a given heating amplitude, the maximum vertical velocity increases as the basic-state wind speed decreases. The maximum vertical velocities in the cases of $U = 2, 3, 4$, and 5 m s^{-1} for $q_0 = 1.2 \text{ J kg}^{-1} \text{ s}^{-1}$ are 1.67, 1.59, 1.39, and 1.11 m s^{-1} , respectively. The nonlinearity factor for thermally induced finite-amplitude waves can be given by (Chun 1991; Lin and Chun 1991)

$$\mu = \frac{gq_0L}{c_pT_0NU^2}, \quad (2)$$

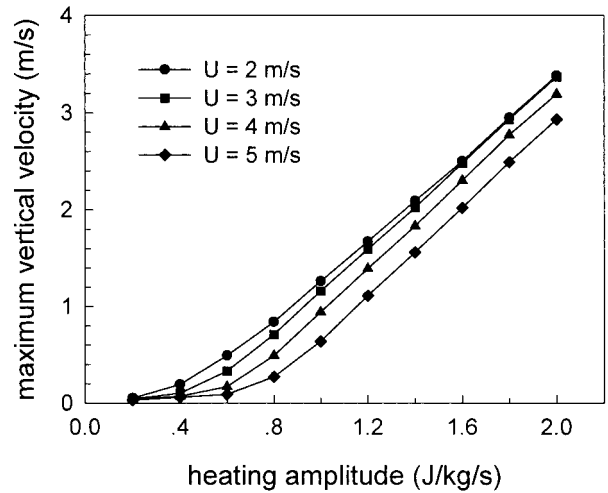
where g is the gravitational acceleration, L is the horizontal length scale of the forcing, and T_0 is the basic-state mean temperature. This nonlinearity factor was derived from a hydrostatic, nonrotating, Boussinesq flow system. The factor μ is proportional to the heating amplitude q_0 and is inversely proportional to the square of the basic-state wind speed U . Therefore, increasing heating amplitude and/or decreasing basic-state wind speed result in increasing nonlinearity in a flow system, that is, increasing perturbation. This relationship helps to explain the variations in the maximum perturbation vertical velocity with changes in the heating amplitude and basic-state wind speed in Fig. 5. The nonlinearity factor also helps to explain the difference between the vertical velocity fields in Fig. 2b ($q_0 = 0.4 \text{ J kg}^{-1} \text{ s}^{-1}$ and $U = 5 \text{ m s}^{-1}$) and Fig. 4b ($q_0 = 0.4 \text{ J kg}^{-1} \text{ s}^{-1}$ and $U = 3 \text{ m s}^{-1}$). There is a weak but identifiable updraft cell downwind of the heating center in the Fig. 4b case (larger nonlinearity), but no downwind updraft cell exists in the Fig. 2b case (smaller nonlinearity factor).

In terms of the heating amplitude and basic-state wind speed, two flow regimes can be identified in dry simulations. One flow regime (open dots in Fig. 6) is characterized only by stationary gravity waves near the heating region. This regime is encountered when the heating amplitude is very small, particularly with large basic-state wind speed, and closely resembles the flow field predicted by linear theory for thermally induced circulation in a stably stratified atmosphere. The other flow regime (filled dots in Fig. 6) is nonlinear and is characterized both by stationary gravity waves near the heating region and by a downwind updraft cell, as illustrated in Figs. 2, 3, and 4.

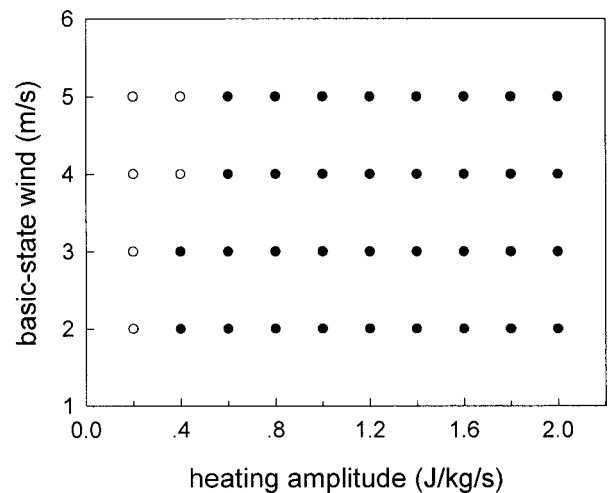
FIG. 3. The time evolution of the perturbation vertical velocity field in a dry simulation with $q_0 = 1.2 \text{ J kg}^{-1} \text{ s}^{-1}$ and $U = 5 \text{ m s}^{-1}$. The perturbation vertical velocity fields are at $t =$ (a) 1, (b) 2, (c) 3, (d) 4, (e) 5, and (f) 6 h. The min and max values and the contour interval (inc) are shown at the bottom of each frame (m s^{-1}).

FIG. 4. The same as Fig. 2 but for $U = 3 \text{ m s}^{-1}$.

The sources (or factors) contributing to the urban heat island, including anthropogenic heat input, are very near the surface, and the heating is then advected and diffused through the atmosphere in reality. Because a spatial form of the temperature perturbation resulting from the urban heat island is specified in this study, there is no true direct coupling between heat flux at/near the

FIG. 5. Domain-maximum perturbation vertical velocity during numerical integration as a function of heating amplitude for basic-state wind speeds of 2, 3, 4, and 5 m s^{-1} .

surface and advection/diffusion processes. For example, under high winds the urban heat island effect would be concentrated nearer the surface; under light winds the heat might diffuse vertically more readily. These effects cannot be captured by the fixed temperature perturbation profile. Because a primary purpose of this study is to examine essential dynamical aspects of convection forced by the urban heat island, the heating profile is prescribed. A further study is needed to take into account feedback between the thermodynamics of the heat island and the dynamics of the atmosphere with a numerical model that is able to treat properly the individual sources responsible for the urban heat island.

FIG. 6. Flow regimes in a parameter space of the heating amplitude and basic-state wind speed (q_0-U) in dry simulations. The open dots represent flow regime characterized only by stationary gravity waves near the heating region; the filled dots represent flow regime characterized by stationary gravity waves near the heating region and a downwind updraft cell.

The results of nonlinear numerical model simulations by Baik (1992) indicate that the downwind updraft cell induced by heating can be quasi-stationary in its horizontal position after some time or can continuously propagate in the downstream direction, depending on the basic-state wind speed. In the current simulations, however, all downwind updraft cells continue to move downstream for all basic-state wind speeds. It is noticed that there are some basic differences between the two model experiments. These are the flow system (hydrostatic, Boussinesq vs nonhydrostatic, compressible), the basic-state wind (shear with no critical level vs uniform), and the specified heating structure. Using the current model, extensive numerical simulations with various wind shears in the absence of a critical level and specified heating structures were performed to discover the main factor that caused the different result in the propagation of the downwind updraft cell. It was found that a widespread cooling term may be responsible for causing the difference. The widespread cooling term, which is added in the specified forcing, is needed to avoid a net heating problem in a steady-state, linear, inviscid flow system (Smith and Lin 1982). This term was retained in the study by Baik (1992). With the widespread cooling term taken into account $\{-ab/[(x-c)^2 + b^2]\}$ is added to the horizontal heating structure function in (1), with $b = 5a$, for example, when the heating amplitude was $1.2 \text{ J kg}^{-1} \text{ s}^{-1}$, the horizontal position of the downwind updraft cell became quasi-stationary for $U = 2$ and 3 m s^{-1} . For both the basic-state wind speeds, its downstream movement was only 3 km over the last 3 h. On the other hand, it was revealed that the downwind updraft cell continues to move downstream when the basic-state wind increases further ($U = 4$ and 5 m s^{-1}). Based upon these results, it is likely that the widespread cooling term acts to retard the propagation of the downwind updraft cell and can make the downwind updraft cell quasi-stationary in its position under certain circumstances.

In dry simulations, the heating amplitude is set to vary from 0.2 to $2 \text{ J kg}^{-1} \text{ s}^{-1}$. For this range of heating amplitudes, the maximum temperature deviation from the basic state in the heating region near the surface (urban heat island intensity) ranges from 0.54°C in the $q_0 = 0.2 \text{ J kg}^{-1} \text{ s}^{-1}$ and $U = 5 \text{ m s}^{-1}$ case to 4.36°C in the $q_0 = 2 \text{ J kg}^{-1} \text{ s}^{-1}$ and $U = 2 \text{ m s}^{-1}$ case. The maximum heat island intensity among the cases that belong to the flow regime only with stationary gravity waves is 1.12°C ($q_0 = 0.4 \text{ J kg}^{-1} \text{ s}^{-1}$ and $U = 4 \text{ m s}^{-1}$). The maximum heat island intensity in the $q_0 = 1.2 \text{ J kg}^{-1} \text{ s}^{-1}$ and $U = 5 \text{ m s}^{-1}$ (3 m s^{-1}) case is 2.35°C (2.83°C). The inverse relation between the heat island intensity and the wind speed is consistent with the result of Oke (1973). Our dry simulation results indicate that the urban heat island, with an intensity of two or more degrees [often found in most big cities; see Oke (1987)], can induce a strong updraft cell downwind of the heat island. Our simulation results also indicate that the in-

tensity of the downwind updraft cell depends on heat island intensity and environmental wind. The downwind updraft cell intensifies and then weakens as it moves downstream. These results suggest that a typical urban heat island can induce a strong updraft cell in its downwind region (dry convection in the absence of moisture) and the urban heat island-induced downwind updraft cell can trigger moist convection and hence cause surface precipitation in favorable environmental conditions. This inspired us to investigate moist convection in various basic-state thermodynamic and wind conditions using a cloud model.

b. Moist simulations

In moist simulations, the heating amplitude varies from 0.2 to $2 \text{ J kg}^{-1} \text{ s}^{-1}$ with increments of $0.2 \text{ J kg}^{-1} \text{ s}^{-1}$ under different environmental conditions. The basic-state wind speed is specified as 3 or 5 m s^{-1} . Five different basic-state thermodynamic states are chosen by changing basic-state relative humidity profile while keeping the basic-state temperature profile the same in all numerical experiments. The five vertical profiles of the basic-state relative humidity are shown in Fig. 1. A total of 100 moist simulations (10 heating amplitudes $\times 2$ basic-state winds $\times 5$ basic-state relative humidity profiles) are performed to characterize moist convection induced by the urban heat island.

Figure 7 shows the cloud water mixing ratio fields at $t = 2, 3$, and 4 h in the $q_0 = 1.2 \text{ J kg}^{-1} \text{ s}^{-1}$, $U = 5 \text{ m s}^{-1}$, and $\text{RH}_L = 90\%$ case. Note that RH_L is the relative humidity in the layer between the surface and $z = 1 \text{ km}$. The rainwater mixing ratio fields corresponding to Fig. 7 are plotted in Fig. 8. In this case, the calculated convective available potential energy (CAPE) for the basic-state thermodynamic soundings is 101 J kg^{-1} when the moisture effect is taken into account. Cloud water is produced for the first time as a result of the condensation of water vapor at $x = 63 \text{ km}$ and $t = 63 \text{ min}$. At this time, the center of the downwind updraft cell induced by the heating is located at $x = 63 \text{ km}$ and its maximum intensity is 0.36 m s^{-1} . Therefore, the horizontal location of cloud formation coincides with that of the center of the downwind updraft cell. This implies that the updraft cell moving in the downstream direction initiated moist convection downstream. Before the cloud forms, the vertical velocity field in the moist simulation is very similar to that in the corresponding dry simulation case because there is no latent heat release yet from the condensation of water vapor.

At $t = 2 \text{ h}$, one single cloud with its top at about 7 km is present (Figs. 7a and 8a) and the surface precipitation has already started (Fig. 8a). Cloud water is predominant over rainwater in the upper region of the cloud, and considerable amounts of both cloud water and rainwater coexist in the middle-to-lower region (Figs. 7a and 8a). The perturbation vertical velocity field at $t = 1 \text{ h } 50 \text{ min}$ showed that downwind of the heating

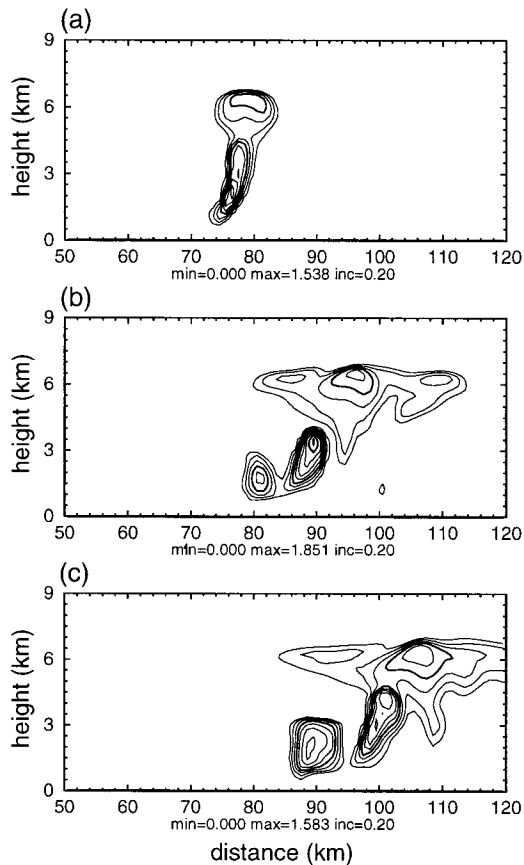


FIG. 7. The fields of the cloud water mixing ratio at $t =$ (a) 2, (b) 3, and (c) 4 h in a moist simulation with $q_0 = 1.2 \text{ J kg}^{-1} \text{ s}^{-1}$, $U = 5 \text{ m s}^{-1}$, and $\text{RH}_L = 90\%$. The min and max values and the contour interval (inc) are shown at the bottom of each frame (g kg^{-1}).

region, above z of about 3 km there exist a strong updraft cell and compensating downdraft cells on both sides of the updraft cell, while below z of about 3 km there is a downdraft due to the falling rainwater and compensating updraft cells on both sides of the downdraft. The compensating updraft cell to the right of the downdraft below z of about 3 km had weakened as it moved downstream. On the other hand, the compensating updraft cell to the left of the downdraft had intensified and split into two updraft cells that are associated with two cloud cells located near $x = 80 \text{ km}$ and 90 km at $t = 3 \text{ h}$ (Fig. 7b). At $t = 3 \text{ h}$, the center of the leading cloud is located at $x = 95 \text{ km}$. This cloud consists mainly of rainwater in the middle-to-lower region and cloud water in the upper region (Figs. 7b and 8b). The upper cloud is characterized by horizontally widespread cloud water (stratiform cloud) having three local maximum regions (Fig. 7b). The second cloud cell behind the leading cloud, whose center is located near $x = 90 \text{ km}$, is composed of cloud water and rainwater (Figs. 7b and 8b). The center of the third cloud cell behind the second cloud cell is located at $x = 81 \text{ km}$ and is composed of cloud water (Fig. 7b). At $t = 4 \text{ h}$, the third cloud cell grows

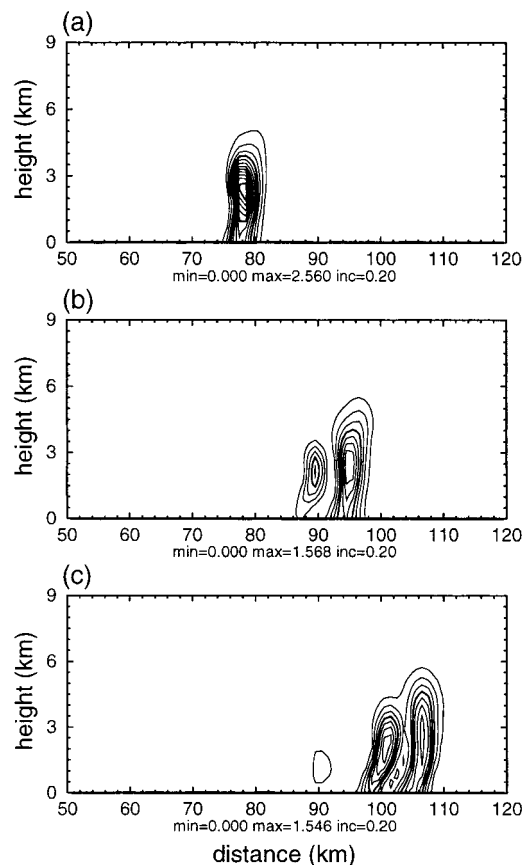


FIG. 8. The same as Fig. 7 but for the rainwater mixing ratio.

and the second cloud is organized with cloud water and rainwater (Figs. 7c and 8c). The leading cloud is well-organized, mainly with rainwater below z of about 4.5 km (Figs. 7c and 8c). In the upper region, the leading and second clouds share a widespread stratiform cloud consisting of cloud water (Fig. 7c), and this stratiform cloud becomes wider with time (Figs. 7b and 7c).

Figure 9a depicts the surface precipitation rate at $t = 2, 3, 4, 5$, and 6 h as a function of horizontal distance in the above simulation case (Fig. 8). The convective precipitating clouds are moving in the downstream direction with a well-defined local precipitation peak (or peaks) at each time. At $t = 2 \text{ h}$, the surface precipitation region is very narrow (8 km) and the peak precipitation rate is as large as 35.8 mm h^{-1} at $x = 77 \text{ km}$. The surface precipitation area becomes wider with time. At $t = 3 \text{ h}$, two local precipitation peaks exist, with the first peak intensity being much larger than the second. Three (four) local peaks in the surface precipitation rate appear at $t = 4 \text{ h}$ (5 h). At the end of the time integration ($t = 6 \text{ h}$), there are two noticeable local precipitation peaks with a horizontal separation distance of 13 km. Figure 9b depicts the accumulated surface precipitation amount over 6 h as a function of horizontal distance in the same simulation case. During the 6-h period, the surface precipitation is detected over the region from x

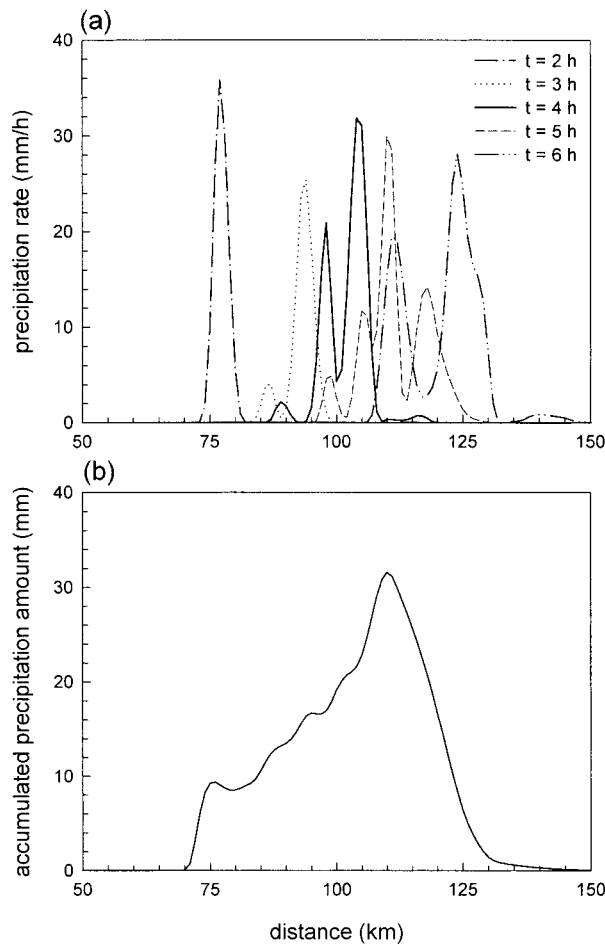


FIG. 9. (a) Surface precipitation rate at $t = 2, 3, 4, 5$, and 6 h and (b) accumulated surface precipitation amount during 6 h as a function of horizontal distance in a moist simulation with $q_0 = 1.2 \text{ J kg}^{-1} \text{ s}^{-1}$, $U = 5 \text{ m s}^{-1}$, and $\text{RH}_L = 90\%$.

$= 70$ km to 150 km. The maximum 6 -h accumulated precipitation amount is 31.6 mm at $x = 110$ km, 60 km away from the heating center. This figure shows that there is a large spatial variation in the accumulated surface precipitation amount.

The rainwater mixing ratio fields at $t = 2, 3$, and 4 h in the $q_0 = 1.2 \text{ J kg}^{-1} \text{ s}^{-1}$, $U = 3 \text{ m s}^{-1}$, and $\text{RH}_L = 90\%$ case are shown in Fig. 10. This case is identical to that of Fig. 8 except that the basic-state wind speed decreases from 5 to 3 m s^{-1} . Here moist convection first starts (first formation of cloud water) at $x = 57$ km and $t = 57$ min. At this time, the center of the downwind updraft cell with its peak intensity of 0.46 m s^{-1} is located at $x = 57$ km. Hence, the horizontal location of cloud formation is the same as that of the center of the downwind updraft cell, implying that the downwind updraft cell initiated moist convection. At $t = 2$ h, an intense rainwater cloud cell is present with its center at $x = 69$ km (Fig. 10a). The cell moves in the downstream direction. At $t = 3$ h, another rainwater cloud cell of lower height and rainwater content is situated upstream

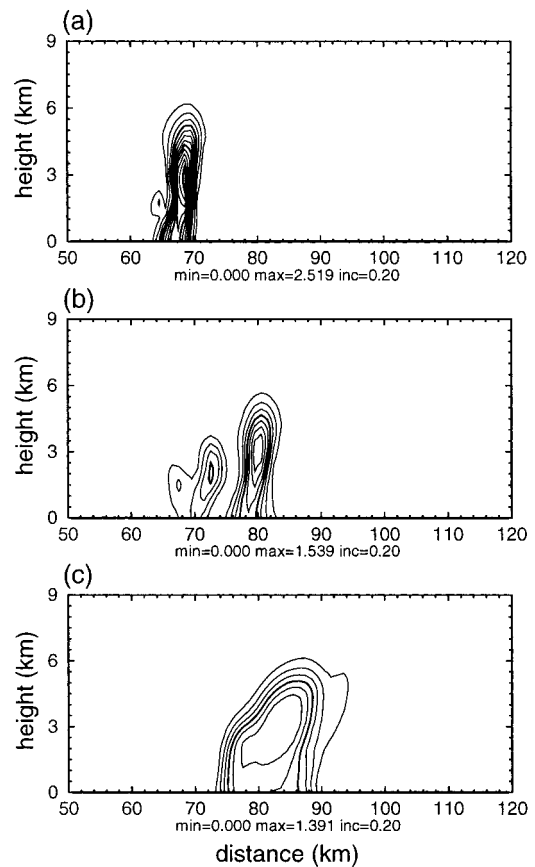


FIG. 10. The fields of the rainwater mixing ratio at $t =$ (a) 2 , (b) 3 , and (c) 4 h in a moist simulation with $q_0 = 1.2 \text{ J kg}^{-1} \text{ s}^{-1}$, $U = 3 \text{ m s}^{-1}$, and $\text{RH}_L = 90\%$. The min and max values and the contour interval (inc) are shown at the bottom of each frame (g kg^{-1}).

of the intense cloud cell (Fig. 10b). At $t = 4$ h, a huge rainwater cloud can be seen (Fig. 10c). The moving speed of the cloud cell is slower than that in the previous case (Fig. 8) because of the decrease in the basic-state wind speed. A comparison of Figs. 8 and 10 demonstrates that the time evolution of cloud morphology and cloud intensity differs if the vertically uniform basic-state wind speed is different.

Figure 11 shows the rainwater mixing ratio fields at $t = 3, 4$, and 5 h in the $q_0 = 1.2 \text{ J kg}^{-1} \text{ s}^{-1}$, $U = 5 \text{ m s}^{-1}$, and $\text{RH}_L = 80\%$ case. This simulation case is the same as that in Fig. 8 except that the basic-state relative humidity is reduced at all heights below $z = 11$ km (see Fig. 1). The CAPE calculated using the given thermodynamic soundings is zero when the moisture effect is included (58 J kg^{-1} when the moisture effect is neglected). Moist convection first begins at $x = 67$ km and $t = 83$ min. At $t = 83$ min, the center of the downwind updraft cell is located at $x = 67$ km and its peak intensity is 0.70 m s^{-1} . The updraft intensity necessary for the triggering of moist convection is about twice that of the $\text{RH}_L = 90\%$ case (0.36 m s^{-1} , Fig. 8) because of the less favorable thermodynamic state for convec-

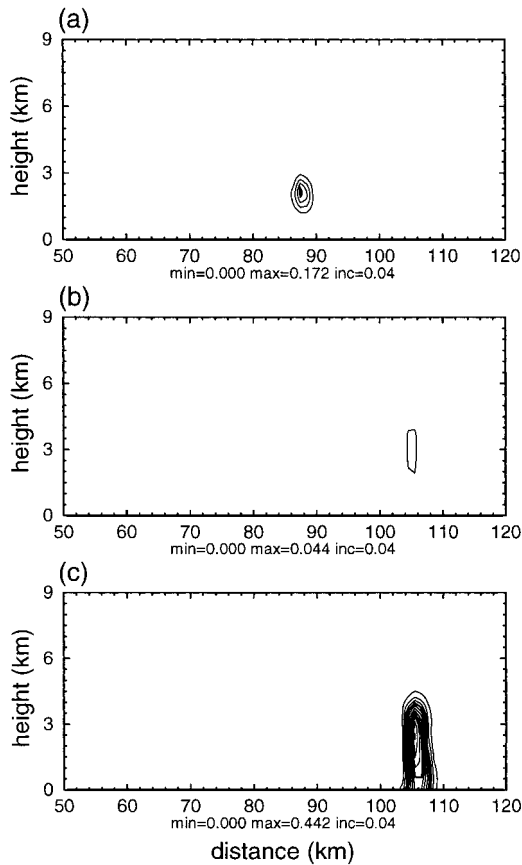


FIG. 11. The fields of the rainwater mixing ratio at $t =$ (a) 3, (b) 4, and (c) 5 h in a moist simulation with $q_0 = 1.2 \text{ J kg}^{-1} \text{ s}^{-1}$, $U = 5 \text{ m s}^{-1}$, and $\text{RH}_L = 80\%$. The min and max values and the contour interval (inc) are shown at the bottom of each frame (g kg^{-1}).

tion. In this simulation case, although the downwind updraft cell forced by the heating does initiate moist convection, water vapor is less abundant and the thermodynamic state of the atmosphere is less favorable for vigorous cloud development. Hence, rainwater first forms 87 min later ($t = 170 \text{ min}$) after the first cloud water formation. At $t = 3 \text{ h}$, a shallow rainwater cloud is situated near $x = 88 \text{ km}$ (Fig. 11a). The rainwater content of the cloud is considerably reduced at $t = 4 \text{ h}$ (Fig. 11b). The rain cloud develops rapidly during the period of $t = 4\text{--}5 \text{ h}$. At $t = 5 \text{ h}$, a well-organized cloud with its height of about 5 km is present near $x = 106 \text{ km}$. However, its maximum rainwater mixing ratio is only 0.44 g kg^{-1} , much less than that at $t = 2 \text{ h}$ in the $\text{RH}_L = 90\%$ case (2.56 g kg^{-1} , Fig. 8a).

An examination of the horizontal location and time of the first cloud water formation downwind of the heating center in the cases corresponding to Figs. 8, 10, and 11 reveals that the horizontal location is farther away from the heating center for the higher basic-state wind speed and that it takes a longer time to form for the lower basic-state relative humidity. Moist simulation results are analyzed in detail to investigate further how

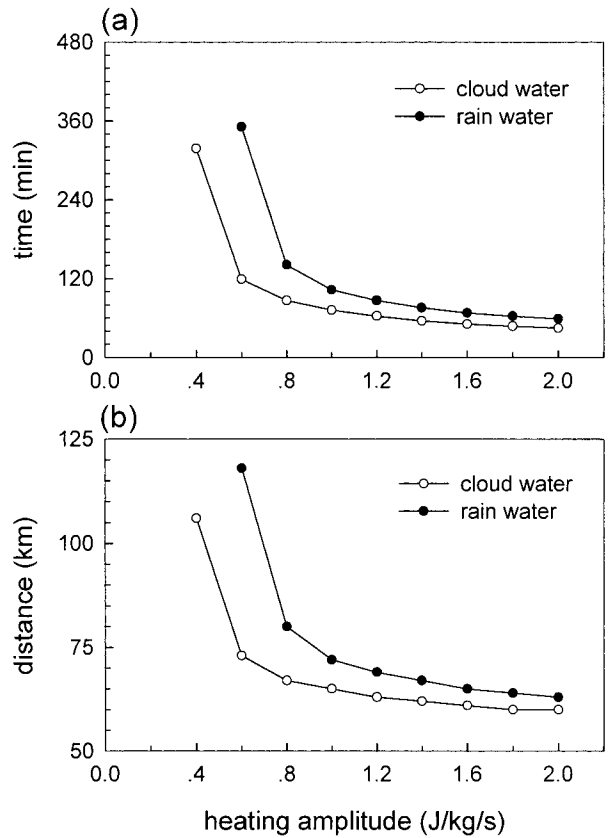
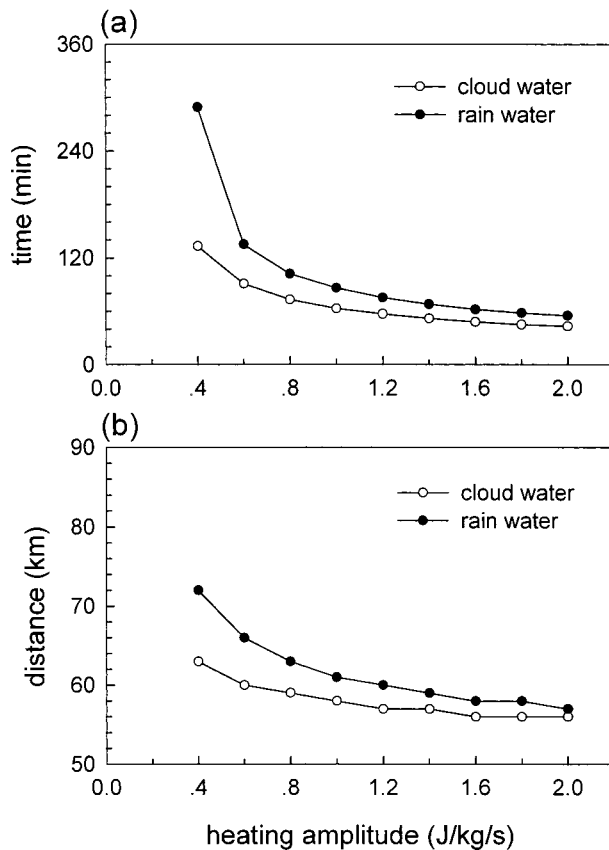
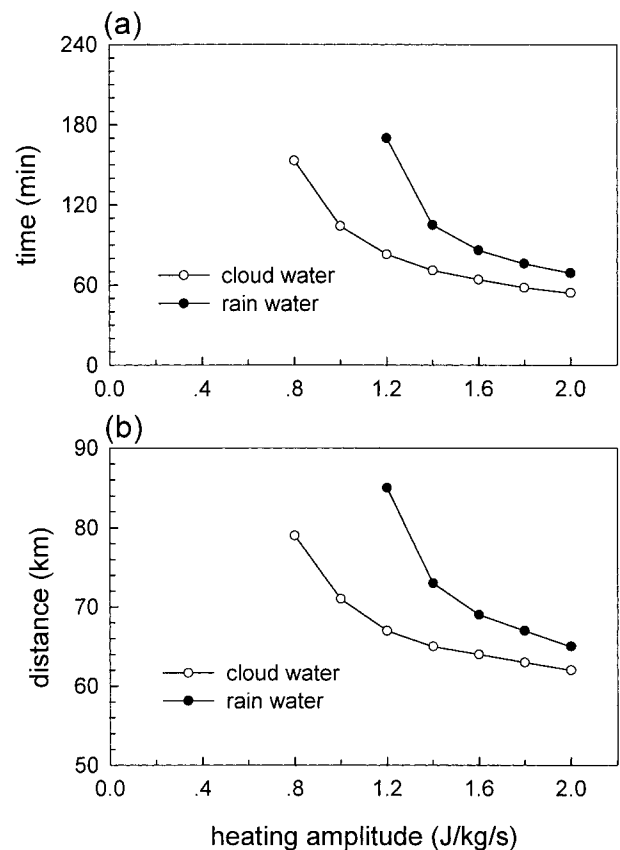


FIG. 12. (a) Time and (b) horizontal location at which cloud water and rainwater are first produced as a function of heating amplitude in moist simulations with $U = 5 \text{ m s}^{-1}$ and $\text{RH}_L = 90\%$.

the time and location of cloud formation depend on heating amplitude and basic-state wind speed and thermodynamic state.

Figure 12 depicts the time and horizontal location at which cloud water and rainwater are first produced as a function of heating amplitude in simulations with $U = 5 \text{ m s}^{-1}$ and $\text{RH}_L = 90\%$. Figure 12a indicates that as the heating amplitude increases, the time required for the first cloud water formation decreases. The variation in the time of the first cloud water formation is more sensitive to small heating amplitude than to large heating amplitude. These results are also true for the rainwater formation. Some time after cloud water forms, an autoconversion process starts that initiates rainwater when the cloud water mixing ratio exceeds a critical value (1 g kg^{-1}). The time required from the first cloud water formation to the first rainwater formation becomes shorter as the heating amplitude becomes larger. It takes 31 min in the $q_0 = 1 \text{ J kg}^{-1} \text{ s}^{-1}$ case, but it takes only 14 min in the $q_0 = 2 \text{ J kg}^{-1} \text{ s}^{-1}$ case. Figure 12b reveals that the horizontal location of the first cloud water formation is farther away from the heating center ($x = 50 \text{ km}$) as the heating amplitude decreases. The variation in the horizontal location of the first cloud water formation is more sensitive to small heating amplitude than

FIG. 13. The same as Fig. 12 but for $U = 3 \text{ m s}^{-1}$.FIG. 14. The same as Fig. 12 but for $\text{RH}_L = 80\%$.

to large heating amplitude. The horizontal location of the first rainwater formation follows the same patterns. The distance between the horizontal location of the first cloud water formation and that of the first rainwater formation decreases as the heating amplitude increases. The distances are 7 and 3 km in the $q_0 = 1$ and $2 \text{ J kg}^{-1} \text{ s}^{-1}$ cases, respectively. In the $q_0 = 0.2 \text{ J kg}^{-1} \text{ s}^{-1}$ case, no cloud water forms, because a downwind updraft cell is absent. In the $q_0 = 0.4 \text{ J kg}^{-1} \text{ s}^{-1}$ case, a downwind updraft cell does not exist, but cloud water forms. However, the beginning of its formation takes place far away from the heating center ($x = 106 \text{ km}$) and near the end of the time integration ($t = 318 \text{ min}$).

In Fig. 13, the basic-state wind speed is reduced from 5 to 3 m s^{-1} with all other parameters kept the same as Fig. 12. The patterns of the time and location of the start of cloud water and rainwater formation with heating amplitude are similar to those in Fig. 12, as described above. With the same heating amplitude, the location of the first cloud water (or rainwater) formation is closer to the heating center and it starts earlier for $U = 3 \text{ m s}^{-1}$ than for $U = 5 \text{ m s}^{-1}$. When the heating amplitude is $0.4 \text{ J kg}^{-1} \text{ s}^{-1}$, only cloud water forms for $U = 5 \text{ m s}^{-1}$ (Fig. 12). On the other hand, both cloud water and rainwater form and cloud water is produced much closer to the heating center for $U = 3 \text{ m s}^{-1}$.

Figure 14 is the same as Fig. 12 except for $\text{RH}_L = 80\%$. The patterns of time and location as a function of heating amplitude are similar to those in Figs. 12 and 13. However, the basic-state thermodynamic state in this case is less favorable for moist convection than that in Fig. 12 or Fig. 13. Hence, a stronger updraft is required to initiate moist convection. Cloud water first forms when the heating amplitude exceeds $0.8 \text{ J kg}^{-1} \text{ s}^{-1}$; rainwater forms when the heating amplitude exceeds $1.2 \text{ J kg}^{-1} \text{ s}^{-1}$.

To get some insight into the dependencies of the dynamic forcing necessary for initiating moist convection on heating amplitude and basic-state wind and thermodynamic state, the maximum downwind updraft at the time that cloud water is first produced is plotted as a function of heating amplitude in Fig. 15. The three curves in this figure correspond to Fig. 12 ($U = 5 \text{ m s}^{-1}$ and $\text{RH}_L = 90\%$), Fig. 13 ($U = 3 \text{ m s}^{-1}$ and $\text{RH}_L = 90\%$), and Fig. 14 ($U = 5 \text{ m s}^{-1}$ and $\text{RH}_L = 80\%$). In all three curves, the maximum downwind updraft at the time of the first cloud water formation increases as the heating amplitude increases. For the same relative humidity profile and heating amplitude, a stronger updraft is needed to initiate moist convection for $U = 3 \text{ m s}^{-1}$ than for $U = 5 \text{ m s}^{-1}$ (cf. the results with $U = 5 \text{ m s}^{-1}$ and $\text{RH}_L = 90\%$ with those with $U = 3 \text{ m s}^{-1}$

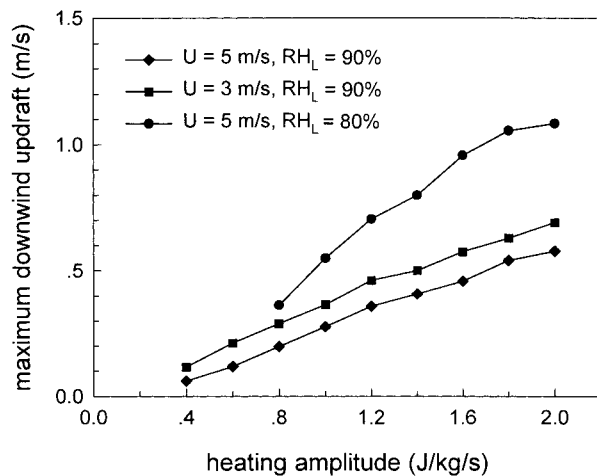


FIG. 15. Maximum downwind updraft velocity at the time of the first cloud water formation as a function of heating amplitude in moist simulations with $U = 5 \text{ m s}^{-1}$ and $RH_L = 90\%$, $U = 3 \text{ m s}^{-1}$ and $RH_L = 90\%$, and $U = 5 \text{ m s}^{-1}$ and $RH_L = 80\%$.

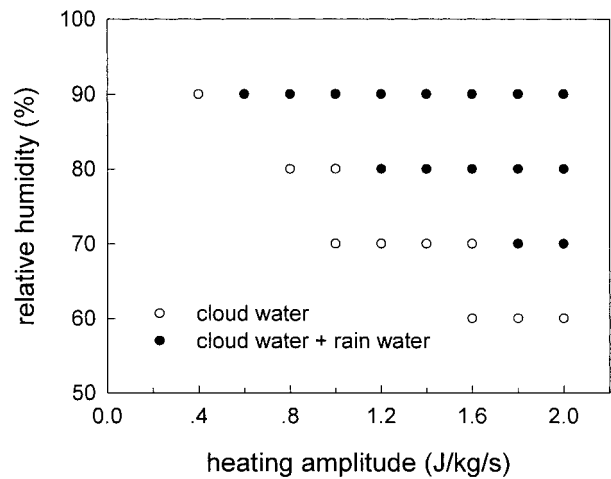


FIG. 16. Hydrometeors that appeared in the moist model atmosphere in a parameter space of the heating amplitude and relative humidity (q_0 - RH_L) for $U = 5 \text{ m s}^{-1}$.

and $RH_L = 90\%$). For the same basic-state wind speed and heating amplitude, a stronger updraft is required for the initiation of moist convection for $RH_L = 80\%$ than for $RH_L = 90\%$ (cf. the results with $U = 5 \text{ m s}^{-1}$ and $RH_L = 90\%$ with those with $U = 5 \text{ m s}^{-1}$ and $RH_L = 80\%$). That is, a stronger dynamic forcing has to exist to trigger moist convection in a less favorable thermodynamic state. The difference in the maximum downwind updraft between the $RH_L = 80\%$ and 90% cases for the same basic-state wind speed of 5 m s^{-1} becomes large as the heating amplitude increases.

Figure 16 shows hydrometeors that appeared in each moist model simulation. This figure is drawn in a parameter space of the heating amplitude and relative humidity for $U = 5 \text{ m s}^{-1}$. As expected, both cloud water and rainwater are produced when the heating amplitude and/or relative humidity are large. On the other hand, the condensation of water vapor does not occur when the heating amplitude and/or relative humidity are small. When RH_L is 50% , there is no condensation of water vapor, because the atmosphere is too dry to support cloud water initiation, even if a strong downwind updraft cell due to the large heating amplitude does exist. For $RH_L = 60\%$, only cloud water is formed when the heating amplitude exceeds $1.6 \text{ J kg}^{-1} \text{ s}^{-1}$. However, the maximum cloud water mixing ratio is only 0.29 g kg^{-1} in the $q_0 = 2 \text{ J kg}^{-1} \text{ s}^{-1}$ case. As RH_L increases further, rainwater starts to be produced. For $RH_L = 90\%$, rainwater forms when the heating amplitude exceeds $0.6 \text{ J kg}^{-1} \text{ s}^{-1}$.

In dry simulations, only stationary gravity waves appear near the heating region when the heating amplitude is $0.2 \text{ J kg}^{-1} \text{ s}^{-1}$ for all basic-state wind speeds and when the heating amplitude is $0.4 \text{ J kg}^{-1} \text{ s}^{-1}$ for $U = 4$ and 5 m s^{-1} (see Fig. 6). In moist simulations with various relative humidity profiles for $U = 5 \text{ m s}^{-1}$, there

is no cloud water formation when the heating amplitude is 0.2 and $0.4 \text{ J kg}^{-1} \text{ s}^{-1}$ except in the $q_0 = 0.4 \text{ J kg}^{-1} \text{ s}^{-1}$ and $RH_L = 90\%$ case (Fig. 16). However, in this case, there exists only cloud water, and its formation is not related to the downwind updraft cell. When the basic-state wind speed is 3 m s^{-1} , there is no cloud water formation for $q_0 = 0.2$ and $0.4 \text{ J kg}^{-1} \text{ s}^{-1}$ except in the $q_0 = 0.4 \text{ J kg}^{-1} \text{ s}^{-1}$ and $RH_L = 90\%$ case (not shown). These results suggest that the weak upward motion downwind of the heating center that is predicted by a linear theory or simulated with very small heating amplitude is not sufficient to initiate moist convection for the given thermodynamic soundings. The downwind updraft cell that has a nonlinear nature is necessary for triggering moist convection.

The results of the moist simulations presented so far suggest that the downwind updraft cell that is thermally induced by the urban heat island can trigger moist convection and result in precipitation in the downstream region if certain environmental conditions necessary to support moist convection are met. The urban heat island-induced downwind updraft cell is a trigger for moist convection. This mechanism can explain the precipitation enhancement observed downwind of urban areas. However, this result should not be interpreted in a way that assigns the urban heat island as a primary cause of downstream precipitation enhancement in all observational cases. There can be observational cases in which the urban heat island is not a dominant cause (Khemani and Murty 1973). The urban heat island in itself implies a spatial variation in temperature between the urban area and its surroundings. Therefore, there always exists a possibility that downstream moist convection and precipitation can take place because of an urban heat island-induced updraft cell if environmental conditions do become favorable.

4. Summary and conclusions

In spite of considerable observational evidence indicating that cities can change or modify local and nearby weather and climate, relatively little attention has been paid to providing an explanation of urban-induced weather and climate from a dynamical viewpoint. This study investigated dry and moist convection forced by an urban heat island through extensive two-dimensional numerical model simulations. For simplicity, the urban heat island was represented by specified heating and the basic-state wind was set to be uniform in the vertical.

In dry simulations, two flow regimes were identified—one exhibiting only stationary gravity waves near the heating region and the other characterized by both stationary gravity waves near the heating region and a downwind updraft cell moving in the downstream direction. The intensity of the downwind updraft cell increased as the heating amplitude (representing the intensity of the urban heat island) increased or the basic-state wind speed decreased. Through extensive moist simulations, it was demonstrated that the downwind updraft cell induced by the urban heat island can initiate moist convection and result in surface precipitation in the downstream region in favorable basic-state thermodynamic conditions. This mechanism may explain the precipitation enhancement observed downwind of urban areas. It was shown that as the urban heat island intensity increases, the time required for the first cloud water (or rainwater) formation decreases and its horizontal location is closer to the heating center. For the same basic-state wind speed and heat island intensity, a stronger dynamic forcing, that is, a stronger downwind updraft cell, was needed to trigger moist convection in a less favorable thermodynamic state.

In this study, in order to isolate the role of the urban heat island in urban-induced convection and precipitation, other potential factors were not considered. One of these is the differences in land use between urban area and its surroundings. In particular, changes in surface roughness can change or modify atmospheric circulation and hence the behavior of convection and precipitation. This needs to be systematically investigated in isolation from and then in connection with urban heat island-induced circulation. In this study, a stable basic-state thermal structure was set in every case. The nocturnal urban heat island generally develops in a stable boundary layer and its intensity is known to be stronger than that of the daytime heat island. The daytime urban heat island, on the other hand, can develop in a nearly neutral boundary layer. This difference in the boundary layer thermal stability can significantly influence heat island circulation (Vukovich and Dunn 1978). The effects of atmospheric thermal stability on urban heat island-induced convection and precipitation deserves in-depth investigation. It is hoped that the current study or similar kinds of studies can provide some valuable dynamical insight for a more thorough understanding of

urban-induced weather and climate in complex real situations.

Acknowledgments. The authors are grateful to anonymous reviewers for providing valuable comments on this study. The authors are also grateful to Kyong-Hee Kim for her early contribution to the urban heat island research. A large portion of this research was performed while the first author was visiting the Department of Applied Mathematics and Theoretical Physics, University of Cambridge, United Kingdom, on his sabbatical leave. He thanks the members of the Fluid Dynamics Group for providing an enjoyable working environment during his stay in Cambridge. This research was supported by the Climate Environment System Research Center sponsored by the SRC Program of the Korea Science and Engineering Foundation. This research was also supported by the Brain Korea 21 Program.

REFERENCES

- Baik, J.-J., 1992: Response of a stably stratified atmosphere to low-level heating—an application to the heat island problem. *J. Appl. Meteor.*, **31**, 291–303.
- , and H.-Y. Chun, 1997: A dynamical model for urban heat islands. *Bound.-Layer Meteor.*, **83**, 463–477.
- , H.-S. Hwang, and H.-Y. Chun, 1999: Transient, linear dynamics of a stably stratified shear flow with thermal forcing and a critical level. *J. Atmos. Sci.*, **56**, 483–499.
- Bornstein, R. D., and G. M. LeRoy, 1990: Urban barrier effects on convective and frontal thunderstorms. *Extended Abstracts, Fourth Conf. Mesoscale Processes*, Boulder, CO, Amer. Meteor. Soc., 120–121.
- , and Q. Lin, 2000: Urban heat islands and summertime convective thunderstorms in Atlanta: Three case studies. *Atmos. Environ.*, **34**, 507–516.
- Changnon, S. A., 1968: The La Porte anomaly: Fact or fiction? *Bull. Amer. Meteor. Soc.*, **49**, 4–11.
- , 1969: Recent studies of urban effects on precipitation in the U.S. *Bull. Amer. Meteor. Soc.*, **50**, 411–421.
- , Ed., 1981: *METROMEX: A Review and Summary*. *Meteor. Monogr.*, No. 40, Amer. Meteor. Soc., 181 pp.
- , R. T. Shealy, and R. W. Scott, 1991: Precipitation changes in fall, winter, and spring caused by St. Louis. *J. Appl. Meteor.*, **30**, 126–134.
- Chun, H.-Y., 1991: Role of a critical level in a shear flow with diabatic forcing. Ph.D. dissertation, North Carolina State University at Raleigh, 159 pp.
- , I.-S. Song, and J.-J. Baik, 1999: Some aspects of internal gravity waves in the multicell-type convective system. *Meteor. Atmos. Phys.*, **69**, 205–222.
- Cotton, W. R., and R. A. Pielke, 1995: *Human Impacts on Weather and Climate*. Cambridge University Press, 288 pp.
- Jauregui, E., and E. Romales, 1996: Urban effects on convective precipitation in Mexico City. *Atmos. Environ.*, **30**, 3383–3389.
- Khemani, L. T., and B. V. R. Murty, 1973: Rainfall variations in an urban industrial region. *J. Appl. Meteor.*, **12**, 187–194.
- Lin, Y.-L., and R. B. Smith, 1986: Transient dynamics of airflow near a local heat source. *J. Atmos. Sci.*, **43**, 40–49.
- , and H.-Y. Chun, 1991: Effects of diabatic cooling in a shear flow with a critical level. *J. Atmos. Sci.*, **48**, 2476–2491.
- Lowry, W. P., 1998: Urban effects on precipitation amount. *Prog. Phys. Geogr.*, **22**, 477–520.
- Oke, T. R., 1973: City size and the urban heat island. *Atmos. Environ.*, **7**, 769–779.

- , 1982: The energetic basis of the urban heat island. *Quart. J. Roy. Meteor. Soc.*, **108**, 1–24.
- , 1987: *Boundary Layer Climates*. 2d ed. Routledge, 435 pp.
- Smith, R. B., and Y.-L. Lin, 1982: The addition of heat to a stratified airstream with application to the dynamics of orographic rain. *Quart. J. Roy. Meteor. Soc.*, **108**, 353–378.
- Vukovich, F. M., and J. W. Dunn, 1978: A theoretical study of the St. Louis heat island: Some parameter variations. *J. Appl. Meteor.*, **17**, 1585–1594.
- Xue, M., K. K. Droegemeier, V. Wong, A. Shapiro, and K. Brewster, 1995: ARPS version 4.0 User's Guide. CAPS, University of Oklahoma, 380 pp.